

Magnon-induced Giant Anomalous Nernst Effect in Single Crystal MnBi

Bin He^{1,2,*}, Cüneyt Şahin^{3,4}, Stephen R. Boona⁵, Brian C. Sales⁶, Claudia Felser¹, Michael E. Flatté^{3,4} and Joseph P. Heremans^{2,7,8}

1. Max Planck Institute for Chemical Physics of Solids, Dresden, Germany, 01187.
2. Department of Mechanical and Aerospace Engineering, The Ohio State University, Columbus OH, 43210, USA.
3. Pritzker School of Molecular Engineering, University of Chicago, Chicago, Illinois, 60637, USA.
4. Optical Science and Technology Center and Department of Physics and Astronomy, The University of Iowa, Iowa City, Iowa, 52242, USA.
5. Center of Electron Microscopy and Analysis, The Ohio State University, Columbus, OH, 43210, USA.
6. Materials Science and Technology Division, Oak Ridge National Lab, Oak Ridge, TN 37830, USA.
7. Department of Materials Science and Engineering, The Ohio State University, Columbus OH, 43210, USA.
8. Department of Physics, The Ohio State University, Columbus, OH, 43210, USA.

Abstract

We present galvanomagnetic and thermoelectric transport measurements on single-crystal MnBi, a rare-earth-free high-temperature permanent magnet material, along different crystallographic directions, and in particular the anomalous Nernst effect in both the in-plane and cross-plane directions. The cross-plane anomalous Nernst thermopower reaches 8 $\mu\text{V}/\text{K}$ at 0.4 T applied field. The anomalous Hall effect also has been measured for both in-plane and cross-plane directions, with opposite signs along different orientations. We attribute this large anomalous Nernst effect to a combination of an intrinsic contribution from the Berry curvature and a new advective magnon contribution arising from magnon-electron spin-angular momentum transfer, which can be viewed as a self-spin Seebeck effect.

Introduction

The anomalous Nernst effect (ANE), which has attracted research attention recently^{1,2} and is the object of this study, is a bulk transport property that is the thermal analog to the anomalous Hall effect (AHE). In contrast, the spin-Seebeck effect (SSE)^{3,4,5,6,7,8} is essentially an advective transport property: a heat flux is applied to a ferromagnetic (FM) insulator or FM metal to create a spin current. The spin current then is injected into an adjacent layer of a normal metal (NM) with high spin-orbit coupling (SOC), for instance, Pt. In the NM layer, the spin flux spin-polarizes the conduction electrons and gives rise to an inverse spin-Hall (ISHE) voltage that is detected. Both the ANE and the SSE are measured in the same geometry⁹, in the ANE case on a homogeneous bulk material and in the SSE case on an FM/NM bilayer, whereby heat and spin fluxes are parallel to each other, but spin flux, spin polarization (or external magnetic field) and detected electric field are orthogonal. Most SSE experiments in the literature use insulating FMs where there is no ANE in order to avoid mixing the two effects. The present study points out that such a clear separation of the two effects may not be possible when studying the ANE in metallic FMs that have a high SOC in bulk, such as MnBi.

The ANE has been observed in FM materials like Fe₃O₄,¹⁰ Fe,¹¹ Co,¹² and MnGe,¹³ and non-collinear antiferromagnets (AFM) including Mn₃Sn.¹⁴ The ANE also has been observed in Dirac semimetals like Cd₃As₂¹⁵ and Weyl semimetals like TaAs¹⁶ and Co₂MnGa¹⁷. A general observation on most known materials, ferromagnetic or not, is that the transverse (Nernst) thermopower generally is of the order of 1 $\mu\text{V/K}$ or less. Several exceptions have been noticed experimentally, e.g., in the FM Heusler compound Co₃Sn₂S₂¹⁸, the anomalous Nernst thermopower reaches 3 $\mu\text{V/K}$ at about 0.2 T, and in

Co_2MnGa ¹⁷, an anomalous Nernst signal has been measured that reaches $6 \mu\text{V/K}$ in a 1 T magnetic field. Among all these materials, a large net Berry curvature near the Fermi level is the dominate mechanism for the ANE. Beyond the intrinsic contribution from Berry curvature, an advective magnon contribution further enhances the ANE thermopower. From this point of view, a FM material with high SOC is an ideal system to study extrinsic ANE mechanism.

MnBi is a FM metal¹⁹ with a high Curie temperature (~ 630 K), making it potentially a high-temperature permanent magnet. In 2014, McGuire et al.²⁰ published a study of single-crystal MnBi that detailed their successful growth using the flux method. There have been several studies of the thermal transport properties of polycrystalline MnBi.^{21,22} Here, we present a giant ANE observed in single-crystal MnBi that reached $8 \mu\text{V/K}$ at 0.4 T magnetic field at 80 K. We examine both the in-plane and cross-plane transport properties. The giant ANE occurs only in the cross-plane direction and is measured on two MnBi single crystals. By *ab-initio* calculation, we confirm that the intrinsic ANE mechanism is not sufficient to explain the observation. We posit that the difference may be due to an additional advective transport process, similar to SSE but in a homogeneous material: the thermally-driven magnon current may spin-polarize the conduction electrons dynamically, which then could result in an additional transverse voltage because of the high SOC in MnBi. We believe this to be the first published data for the transport properties of single-crystal MnBi from 80 K to 300 K.

Experiments

Single crystals of MnBi were grown at Oak Ridge National Lab using the method

detailed in McGuire et al.²⁰ MnBi single crystals grow as hexagonal cylinders, and the c -axis can be determined by its attraction to a permanent magnet at room temperature. We measured the transport properties in a modified Janis liquid nitrogen flow cryostat. A temperature gradient was applied on one side of the sample; two thermocouples were placed along the applied temperature gradient to measure it and the voltage. Current wires were affixed to the heater and heat sink for electrical measurements. Two copper wires were attached to the back side to measure the Hall and Nernst signals. The temperature range for transport measurements is 80 K \sim 300 K, and the maximum field is 1.4 T. We started with one cross-plane crystal labeled A1 and one in-plane crystal labeled B1, and we observed a giant ANE on A1. To verify our giant ANE thermopower, we measured a second cross-plane sample, A2. All the measurements are taken under adiabatic condition.

We use the following notation for the transverse transport properties, which are denoted by indices xyz . Here, x is the direction of the applied thermodynamic flux (charge or heat flux), y is the direction of the measured voltage or temperature gradient, and z is the field direction. Thus, S_{xyz} is the in-plane Nernst thermopower with the magnetic field along the z $[0,0,1]$ axis and measured on crystal B1, while S_{zxy} is the cross-plane Nernst thermopower with the field in-plane and measured on crystals A1 and A2. The Seebeck coefficients are S_{zz} on A1 and A2, and S_{xx} on B1.

Results

Fig. 1(a) shows the crystal structure of MnBi, viewed from the c -axis. It has the NiAs structure, with the Mn as the smaller purple ball and Bi as the larger blue ball. Fig. 1(b) and 1(c) shows the spin reorientation in MnBi crystals. Previous neutron diffraction

results²⁰ on those crystals showed a spin reorientation starts at $T_{SR}=90$ K, with a symmetry-lowering phase transition that moves from a hexagonal to an orthorhombic structure. Below 90 K, the spins are aligned in-plane, as shown in Fig. 1(b). Above 140 K, the spins are aligned along the c -axis, as shown in Fig. 1(c). This spin-reorientation process has a critical influence on the magnon band structure of MnBi, and thus affect the transport properties.

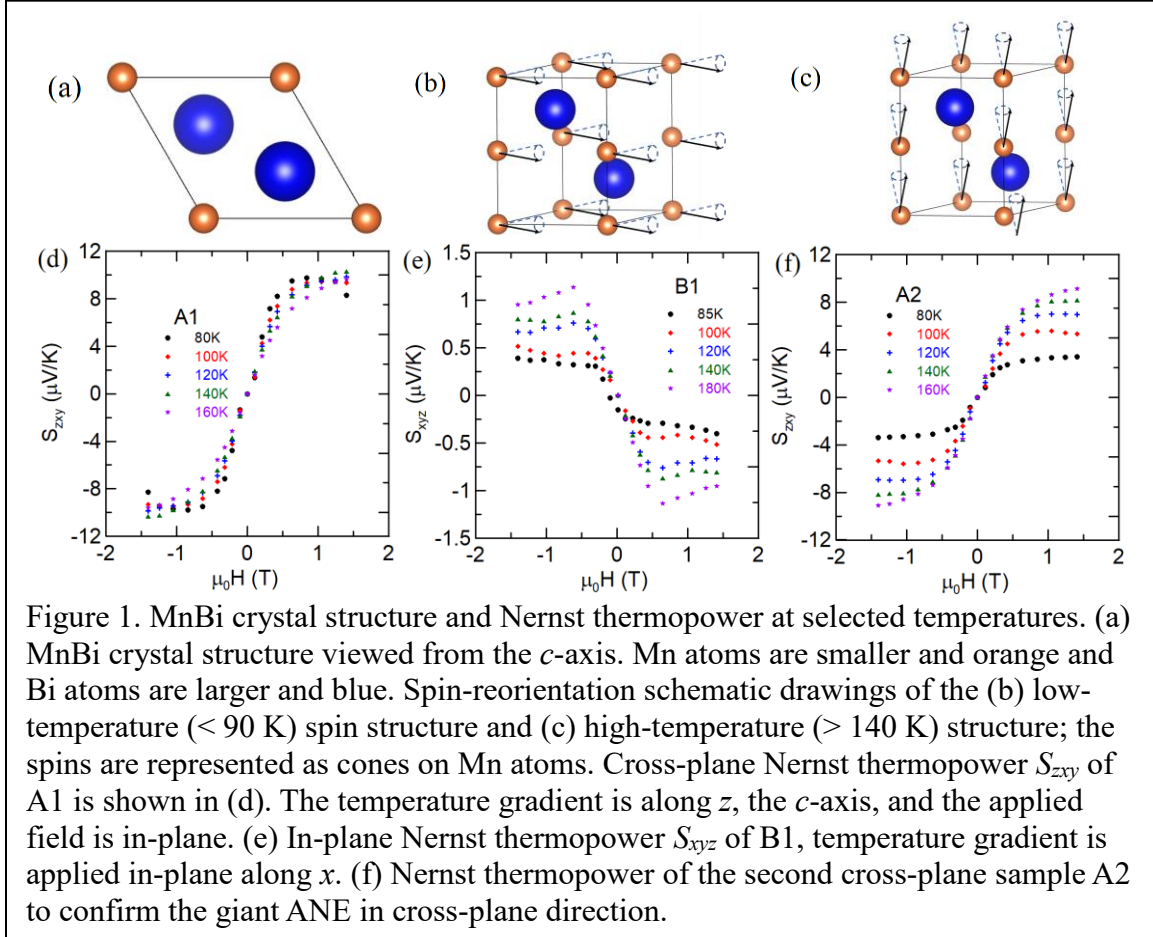


Fig. 1(d) and (e) show the cross-plane and in-plane Nernst thermopower S_{zxy} and S_{xyz} on samples A1 and B1 at various temperatures, respectively. A clear ANE is observed on both samples. The Nernst effect S_{xyz} can be separated into two parts, the ordinary Nernst effect (ONE) and the ANE, where $S_{xyz} = S_{xyz,ONE} + S_{xyz,ANE}$ and equivalent for S_{zxy} . In MnBi, the ANE dominates the low-field region, up to 0.4 T, and the ONE dominates the high-field

region, where the magnetization is saturated²⁰. In both samples at higher field, the ANE slope is significantly larger than the ONE slope, which is close to zero for A1. With the high-field ONE coefficient for A1 being negligible, we take the low-field Nernst thermopower as the contribution of the ANE. We observed that from 80 K to 160 K, where the spin reorientation happens, the ANE did not change significantly with temperature and is $S_{zxy, ANE} \sim 8 \mu\text{V/K}$ at a field of 0.4 T at 80 K. Conversely, the Nernst thermopower in sample B1 has a different sign from the cross-plane measurement, the value of which changes from $S_{xyz, ANE} \sim -0.3 \mu\text{V/K}$ to $-1 \mu\text{V/K}$, comparable to many metallic ferromagnets²³. We also observe a sign change in the ONE in the in-plane direction, possibly coming from a changing in the scattering mechanism²⁴ during the spin reorientation. To confirm the giant ANE signal, we repeat the cross-plane Nernst measurement on a second sample A2. Again, we observe a giant ANE signal. Compared to A1, A2 shows an obvious temperature dependence with the ANE thermopower increasing with temperature from $2.7 \mu\text{V/K}$ at 80 K to $6 \mu\text{V/K}$ at 140 K. Their different temperature dependence will be discussed in the next part. Nevertheless, the maximum ANE thermopower of sample A1 and A2 are close to each other, showing good reproducibility. The giant ANE thermopower we achieved from both cross-plane samples are comparable or higher than that of Co_2MnGa , which is considered to have the largest ANE response.

A large ANE is often believed related to a large AHE. Fig. 2(a) and (b) show the Hall resistivities ρ_{zxy} of sample A1 and A2 at selected temperatures. The ρ_{zxy} of the two samples is dominated at low field by the AHE because both samples exhibit a sign change of the slope $d\rho_{zxy}/dH_x$ at ~ 0.4 T across all temperatures. Starting from the measured field-dependent resistivity, we subtract the high-field linear part, and we can calculate the

anomalous Hall conductivity (AHC) with the formula $\sigma_{xz} = \rho_{zx} / (\rho_{zz}\rho_{xx} + \rho_{zx}^2) \approx \rho_{zx} / \rho_{zz}^2$. Since ρ_{zx} is an order of magnitude smaller than ρ_{zz} , we can use the approximation to calculate the Hall conductivity at various temperatures with the resistivity (shown in Fig. 3(a) with MR in Fig. S2). Fig. 2(c) shows the temperature dependent AHC of A1 and A2 at 0.4 T. The AHC σ_{xzy} of A1 is almost an order of magnitude higher than A2. From Fig. 2(a) and (b), the Hall resistivity of A1 and A2 are close to each other, so that the difference in AHE arises from different resistivities. The AHC of sample A1 is comparable to some high-AHC materials²⁵.

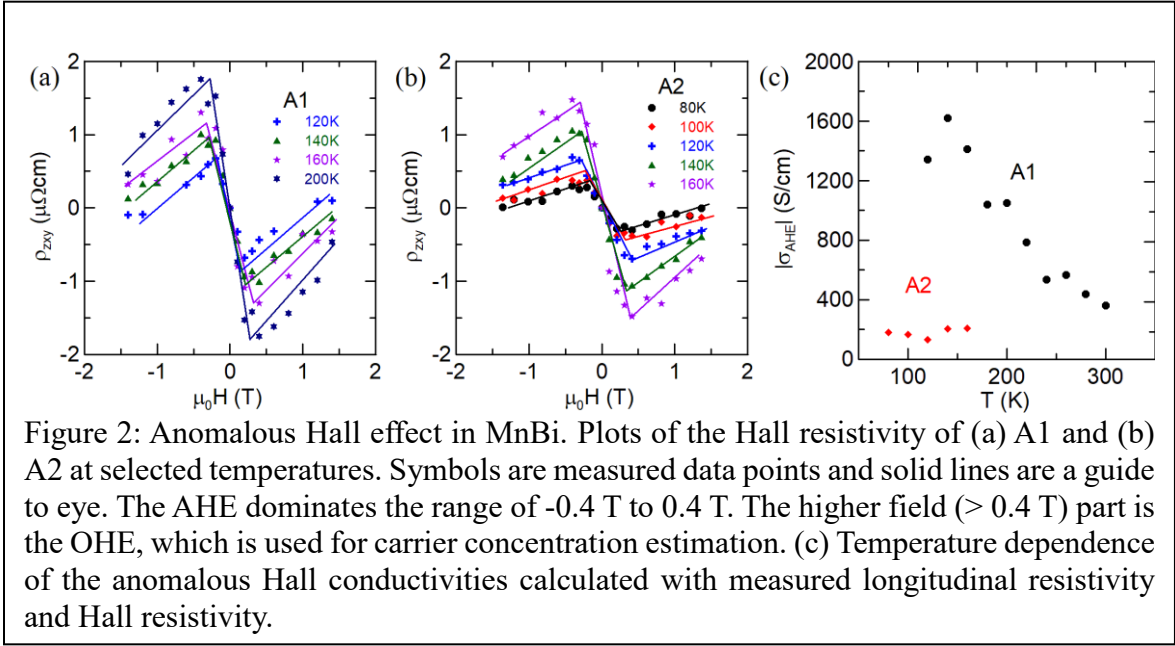
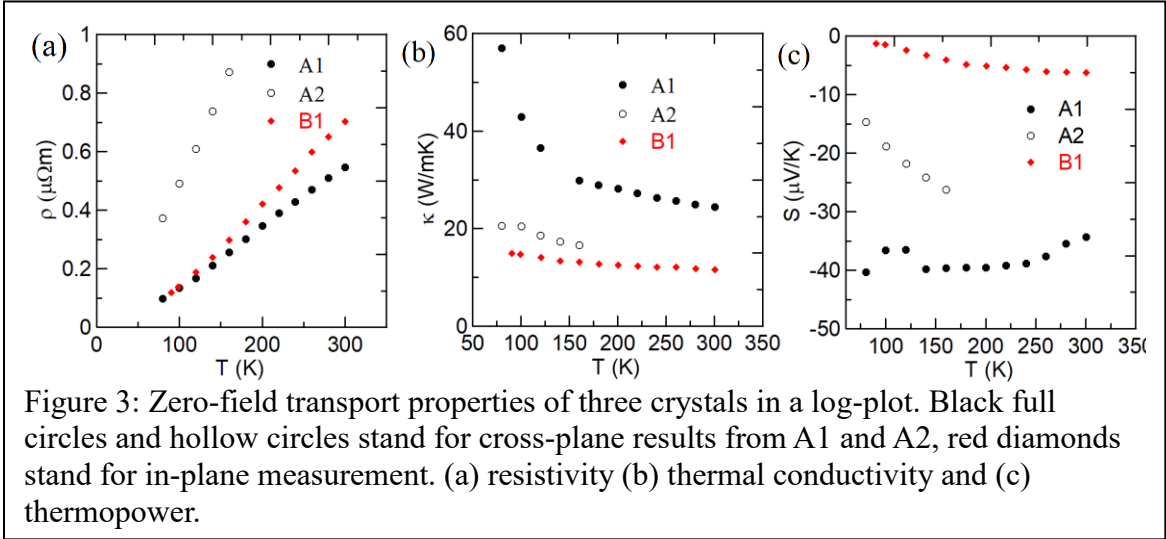


Figure 2: Anomalous Hall effect in MnBi. Plots of the Hall resistivity of (a) A1 and (b) A2 at selected temperatures. Symbols are measured data points and solid lines are a guide to eye. The AHE dominates the range of -0.4 T to 0.4 T. The higher field (> 0.4 T) part is the OHE, which is used for carrier concentration estimation. (c) Temperature dependence of the anomalous Hall conductivities calculated with measured longitudinal resistivity and Hall resistivity.

Fig. 3(a) and (b) show the zero-field resistivity and thermal conductivity of all three samples, respectively. The resistivity of all three samples are linear in temperature, indicative of metallic behavior. The resistivity of A1 and B1 are close to each other, which is about a third of A2, indicating that A1 should have a better crystallinity and fewer defects. We believe the difference is coming from the partial oxidation of sample as MnBi is air

sensitive. The same phenomenon has been observed in the thermal conductivity as well, from which we observed that the thermal conductivity of A2 is a third of A1. The thermopower of the three crystals are shown in Fig. 3(c). As A1 is supposed to have less defects and thus a smaller carrier density, A1 displays a higher thermopower than A2, as expected from the Mott formula.²⁶ Moreover, the temperature dependence of A2 shows metallic behavior, while the thermopower of A1 decreases slightly with temperature, indicating the presence of a possible magnon-drag contribution. We notice that the slope of the ordinary part of the Hall effect (OHE) is positive, while the thermopower of MnBi is negative. In metals, the opposite signs can arise from a multi-carrier effect,²⁷ which would give rise to a transverse thermopower that is higher than longitudinal thermopower.²⁸ However, that is not the case in MnBi. In this case, the different signs of the thermopower and Hall coefficient is possibly arising from the geometry of the Fermi surface²⁹.



Discussion

The ANE is related to the energy derivative of the AHE via the Mott relation^{26,30} in metals and degenerately doped semiconductors, as long as the carriers in those materials are

at thermodynamic equilibrium. This relation permits the calculation of an intrinsic contribution to the ANE that has the same origin as that of the AHE. The origin of the intrinsic AHE, elucidated clearly in the past decade,³¹ is a net Berry curvature in the electron wavefunction, while additional extrinsic contributions are attributed to skew-scattering and side-jump. Advective contributions to both the ordinary and anomalous Nernst effects can also arise in thermoelectric transport from interactions between charge carriers and quasi-particles, including magnon drag,³² paramagnon drag,³³ and phonon drag³⁴. The Mott relation breaks down in the presence of drag contributions³⁵ because the Mott formula assumes a required electron energy distribution that follows equilibrium Fermi-Dirac statistics;²⁶ under drag conditions, the electron population taken in isolation is not at equilibrium. We derive the experimental thermoelectric conductivity tensor elements, in particular the experimental anomalous Nernst conductivity (ANC) components α_{xyz} and α_{zxy} , at various temperatures. The thermoelectric conductivity tensor α is related to the thermopower tensor \mathbf{S} and the conductivity tensor σ , and in particular, the transverse element $\alpha_{xy} = S_{xx}\sigma_{yx} + S_{xy}\sigma_{xx}$. Fig. 4(a) shows the experimental ANC of all 3 samples derived from the thermopower, Nernst, conductivity and Hall data by the formula above; when the anomalous Hall conductivity is unavailable experimentally, the first term is ignored, due to its relatively small contribution to the total anomalous Nernst conductivity. The cross-plane ANCs are significantly higher than the in-plane ANC due to a much higher ANE thermopower. On both sample A2 and sample B1, we observe a turnover of the ANC around 140 K, at which temperature spins are aligned along the c -axis. At the same time, we observe a different temperature dependence of the two cross-plane crystals, A1 and A2. The ANC of A2 does not change much with temperature, while the ANC of A1 monotonically decreases

with temperature, which is quite different from most ferromagnets. Moreover, the ANC in crystal A1 is an order of magnitude higher than known materials with large ANE effect. Thus, it is likely that there is an additional contribution to the total ANC, which we posit is an advective effect like magnon-drag and SSE³⁵.

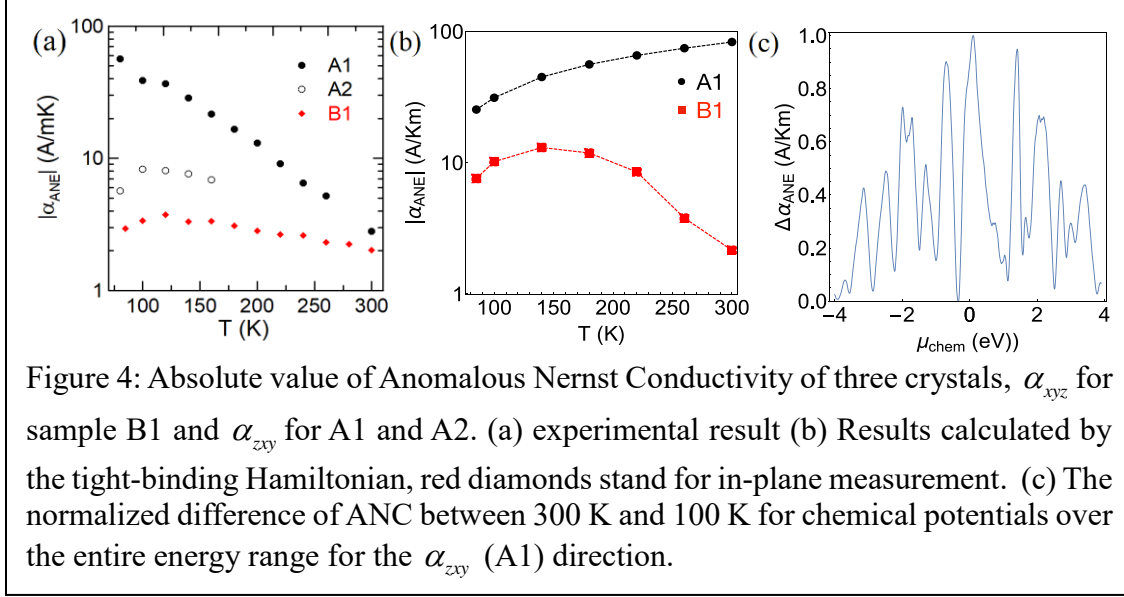


Fig. 4(b) shows the calculated ANCs of one in-plane and one out-of-plane configuration, corresponding to samples A1 and B1. The intrinsic contribution to the ANC is related to the sum of the Berry curvatures and can be calculated from the well-established relation:³⁶

$$\alpha_{ij} = -\frac{1}{e} \int d\varepsilon \frac{\partial f(\varepsilon)}{\partial \mu} \sigma_{ij}(\varepsilon) \frac{\varepsilon - \mu}{T}$$

where e is the electric charge, f is the Fermi-Dirac distribution, T is the temperature, σ denotes the energy resolved intrinsic AHC, and μ is the chemical potential. The energy-resolved AHC is calculated from integrating the Berry curvatures

$$\sigma_{ij} = -\frac{e^2}{\hbar} \int d\mathbf{k} \sum_n \Omega_{ij}(n\mathbf{k}) f_{n\mathbf{k}}$$

where Ω_{ij} is the Berry curvature, and the sum is performed over all occupied bands in the first Brillouin zone. We first construct a tight-binding Hamiltonian using the parameters derived from the DFT.³⁷ MnBi crystal has a point group of D_{6h} and a space group of P63, with a hexagonal crystal structure and 4 atoms per unit cell. The lattice constants are taken as $a=b=4.285$ Å and $c=6.113$ Å. The tight-binding Hamiltonian consist of p-orbitals of bismuth and d-orbitals of manganese. The magnetism is incorporated into the Hamiltonian through the Stoner formalism with parameters as 4.5 eV and 0.2 eV for d- and p-orbitals, respectively. We also have added the spin-orbit Hamiltonian with spin-orbit couplings of 0.048 eV and 1.4 eV for Mn and Bi, respectively. The Berry curvature, which is an intrinsic property of the electronic band structure, then is computed from this 16-band tight-binding Hamiltonian using the equation:

$$\Omega_{ij}(nk) = Im \sum_{n \neq n'} \frac{\langle u_{nk} | \frac{\partial H}{\partial k_i} | u_{n'k} \rangle \langle u_{n'k} | \frac{\partial H}{\partial k_j} | u_{nk} \rangle}{(\epsilon_n - \epsilon_{n'})^2}$$

For zero magnetization (or no external magnetic field) d-orbitals are located densely around 0 eV energy. As magnetization is increased with applied field, bands that predominantly consist of d-orbitals move away from the center to higher and lower energies. The general behavior of the calculated intrinsic ANC is similar for both α_{zy} (A1) and α_{yz} (B1) up to 150 K, increasing with increasing temperatures as shown in Fig. 4(b) for a chemical potential around 1 eV. The calculated ANC for the α_{yz} (B1) in-plane direction decreases after 150 K consistent with the experimental measurements shown in Fig. 4(a) whereas ANC of the A1 direction continues to increase with the temperature. In order to verify the robustness of this behavior, we performed ANC calculations for the entire range of the chemical potentials from the lowest to the highest possible energy values

as plotted in Fig. 4(c). We take the difference of the ANC at 300 K and 100 K temperatures as a function of the chemical potential and normalize it with the highest such difference. We conclude that the intrinsic ANC for A1 direction is always larger in magnitude at higher temperatures independent of where the chemical potential is located; thus, the intrinsic contribution does not explain the behavior of the decreasing ANC with increasing temperature sufficiently by itself for the α_{xy} (A1) direction.

Therefore, we raise the possibility that an additional advective transport mechanism might contribute to the large ANC signal and the strange behavior of its sign. One transport mechanism that might do this is a hybrid between magnon drag and the spin-Seebeck effect, which share the same geometry.^{9,38} A magnon spin current can be driven thermally by an applied temperature gradient, and the magnons thereby can acquire a linear momentum and spin-angular momentum. The transfer of linear momentum between magnons and electrons is recognized as the magnon-drag effect, which generates a very large, often dominant, contribution to the thermopower.^{11,39} Here, we propose that magnon spin flux in the metallic FM can transfer spin-angular moment to the itinerant electrons during magnon-electron scattering in the bulk of the FM itself, thereby spin polarizing them dynamically over what can be expected from the equilibrium band structure. This idea corresponds to spin pumping across an interface in SSE, except that here the spin pumping would occur in the bulk during scattering processes. This electron polarization then can generate a transverse electric field $E_{ISHE} = D_{ISHE} (J_S \times \sigma)$ where D_{ISHE} stands for the efficiency of the ISHE, and is determined by the intensity of the spin-orbit coupling (SOC). Overall, this additional contribution to the ANE could be labeled a self-SSE term. Bi is known to exhibit the largest SOC,⁴⁰ which allows MnBi to have a large D_{ISHE} , giving rise to a potentially

large contribution to the ANE seen in sample A1.

The observed temperature dependence gives further evidence that points toward this interpretation. At low temperature, the local spins are in the $[1,0,0]$ direction, and ΔT is applied along the $[0,0,1]$ direction. The temperature gradient can excite the magnons and give rise to the self-SSE after applying an external field. In this case, the self-SSE is the origin of the giant Nernst thermopower in α_{zy} (A1). Between 90 K and 140 K, the local spins start to rotate from $[1,0,0]$ to $[0,0,1]$, along with the change of magnon band structure. The spin orientation reduces the total number of magnons excited by the temperature gradient along the $[0,0,1]$ direction, so that the self-SSE signal should decrease with temperature, while the intrinsic contribution increases with temperature. The combination of these two factors gives rise to the ANE thermopower to be constant during the spin reorientation. We propose that, except for the D_{ISHE} , this new self-SSE mechanism should depend on the same materials parameters as determine the magnon-drag thermopower, since both involve a thermally driven spin flux and electron-magnon scattering. These are the charge-carrier concentration, the magnon specific heat, and the ratio between total magnon scattering time and magnon-electron scattering time.¹¹ Crystal quality plays an important role in magnon lifetime. As discussed above, crystal A2 has a higher defect concentration than crystal A1, so that the drag effect is smaller in crystal A2, with its ANE thermopower smaller and increasing linearly with temperature. Data on the effect of thermal cycling on the results on the ANE are shown in the supplement and illustrate that the effect decreases as the sample sustains damage, possibly as a result of increased magnon-defect scattering.

Conclusion

In summary, we measured the transport properties of MnBi single crystals, and observed a giant ANE in the cross-plane measurement at low temperature. This giant anomalous Nernst signal can be attributed to a combination of intrinsic Berry curvature and what we posit is an advective contribution resulting from a thermally driven magnon flux that induces an additional transverse voltage similar to the SSE, but intrinsic to the sample. Anisotropy is observed in both thermopower and thermal conductivity. The giant anomalous Nernst thermopower we detected is $8 \mu\text{V/K}$ at 0.4 T, larger than any reported results.

Acknowledgements

The work at OSU is supported by the Center for Emerging Materials, an NSF MRSEC grant DMR-2011876. The work at MPI CPfS is supported by ERC TOPMAT, the European Union (grant No. 742068) and European Union's Horizon 2020 research and innovation program (grant No. 766566). C.Ş. and M.E.F. acknowledge support from the Center for Emergent Materials, an NSF MRSEC under Award No. DMR-1420451.

The work at Oak Ridge (crystal growth). was supported by the U.S. Department of Energy, Office of Science, Basic Energy Sciences, Materials Sciences and Engineering Division.

References

- ¹ A. Sakai et al., Giant anomalous Nernst effect and quantum critical scaling in a ferromagnetic semimetal, *Nat. Phys.* **14**, 1119-1124 (2018).
- ² A. Sakai, et al., Iron-based binary ferromagnets for transverse thermoelectric conversion, *Nature* **581**, 53–57 (2020).
- ³ K. Uchida et al., Observation of the spin Seebeck effect, *Nature* **455**, 778–781 (2008).
- ⁴ K. Uchida et al., Spin Seebeck insulator, *Nat. Mater.* **9**, 894–897 (2010).
- ⁵ C. M. Jaworski et al., Giant spin Seebeck effect in a non-magnetic material, *Nature* **487** 210-213 (2012).
- ⁶ K. Uchida et al., Long-range spin Seebeck effect and acoustic spin pumping, *Nat. Mater.* **10**, 737-741 (2011).
- ⁷ C. M. Jaworski et al. Spin-Seebeck effect: A phonon driven spin distribution, *Phys. Rev. Lett.* **106**, 186601 (2011).
- ⁸ C. M. Jaworski et al., Observation of the spin-Seebeck effect in a ferromagnetic semiconductor, *Nat. Mater.* **9**, 989-902 (2010).
- ⁹ K. Vandaele, et al., Thermal Spin Transport and Energy Conversion, *Mater. Today Phys.* **1** 39-49 (2017)
- ¹⁰ R Ramos et al., Anomalous Nernst effect of Fe₃O₄ single crystal, *Phys. Rev. B* **90**, 054422 (2014)
- ¹¹ S. J. Watzman et al., Magnon-drag thermopower and Nernst coefficient in Fe, Co, and Ni, *Phys. Rev. B* **94**, 14 (2016).
- ¹² T. C. Chuang et al., Enhancement of the anomalous Nernst effect in ferromagnetic thin films, *Phys. Rev. B* **96**, 174406 (2017).

-
- ¹³ Y. Shiomi et al., Topological Nernst effect in a three-dimensional skyrmion-lattice phase, *Phys. Rev. B* **88**, 064409 (2013).
- ¹⁴ M. Ikhlas et al., Large anomalous Nernst effect at room temperature in a chiral antiferromagnet, *Nat. Phys.* **13**, 1085-1090 (2017).
- ¹⁵ T. Liang et al., Anomalous Nernst Effect in the Dirac Semimetal Cd₃As₂, *Phys. Rev. Lett.* **118**, 136601 (2017).
- ¹⁶ F. Caglieris et al., Giant anomalous Nernst effect in Weyl semimetals TaP and TaAs, *Phys. Rev. B* **98**, 201107(R) (2018).
- ¹⁷ S. N. Guin et al., Anomalous Nernst effect beyond the magnetization scaling relation in the ferromagnetic Heusler compound Co₂MnGa, *NPG Asia Mater.* **11**, 16 (2019).
- ¹⁸ S. Guin et al., Zero-field Nernst effect in a ferromagnetic Kagome-lattice Weyl-semimetal Co₃Sn₂S₂, *Adv. Mater.* **31**, 186022 (2019).
- ¹⁹ E. Adams et al., A new permanent magnet from powdered manganese bismuthide, *J. Appl. Phys.* **23**, 1207 (1952).
- ²⁰ M. A. McGuire et al., Symmetry-lowering lattice distortion at the spin reorientation in MnBi single crystals, *Phys. Rev. B* **90**, 174425 (2014).
- ²¹ N. Poudyal and J. P. Liu, Advances in nanostructured permanent magnets research, *J. Phys. D: Appl. Phys.* **46**, 043001 (2013).
- ²² H. J. Williams et al., Magnetostriction and magnetic anisotropy of MnBi, *J. Appl. Phys.* **28**, 445 (1957).

-
- ²³ J. Weischenberg et al., Scattering-independent anomalous Nernst effect in ferromagnets. *Phys. Rev. B* **87**, 060406 (2013)
- ²⁴ E. H. Putley, *The Hall effect and Semiconductor physics*, Dover Publications Inc., New York 1968.
- ²⁵ L., Kang, M., Liu, J. et al., Massive Dirac fermions in a ferromagnetic kagome metal, *Nature* **555**, 638–642 (2018).
- ²⁶ M. Cutler and N. F. Mott, Observation of Anderson localization in an electron gas, *Phys. Rev.* **181**, 1336 (1969).
- ²⁷ V. Jovovic and J. P. Heremans, Measurements of the energy band gap and valence band structure of AgSbTe₂, *Phys. Rev. B* **77**, 245204 (2008).
- ²⁸ S. J. Watzman et al., Dirac dispersion generates unusually large Nernst effect in Weyl semimetals. *Phys. Rev. B* **97**, 161404 (2018).
- ²⁹ N. P. Ong, Geometric interpretation of the weak-field Hall conductivity in two-dimensional metals with arbitrary Fermi surface. *Phys. Rev. B* **43**, 193 (1991).
- ³⁰ Y. Pu et al., Mott relation for anomalous Hall and Nernst effects in Ga_{1-x}Mn_xAs ferromagnetic semiconductors, *Phys. Rev. Lett.* **101**, 117208 (2008).
- ³¹ N. Nagaosa et al., Anomalous Hall effect, *Rev. Mod. Phys.* **82**, 1539-1592 (2010).
- ³² F. J. Blatt et al., Magnon-drag thermopower in iron, *Phys. Rev. Lett.* **18** 395 (1967).
- ³³ Y. Zheng et al., Paramagnon drag in high thermoelectric figure of merit Li-doped MnTe, *Sci. Adv.* **5** eaat9461 (2019).
- ³⁴ J. M. Ziman, *Electrons and Phonons*, Clarendon Press, Oxford (1960).
- ³⁵ J. P. Heremans, Thermal spin transport and spin in thermoelectrics, arXiv:2001.06366, *La Rivista del Nuovo Cimento* (accepted, 2020).

-
- ³⁶ D. Xiao et al., Berry-phase effect in anomalous thermoelectric transport, *Phys. Rev. Lett.* **97**, 026603 (2006).
- ³⁷ K. V. Shanavas et al., Theoretical study on the role of dynamics on the unusual magnetic properties in MnBi *Sci. Rep.* **4**, 7222 (2014).
- ³⁸ S. R. Boona et al., Observation of spin Seebeck contribution to the transverse thermopower in Ni-Pt and MnBi-Au bulk nanocomposites, *Nat. Commun.* **7**, 13714 (2016).
- ³⁹ Y. Zheng et al., Magnon drag effect in Fe-Co alloys, *J. Appl. Phys.* **26**, 12 (2019).
- ⁴⁰ J. P. Heremans et al., Tetradymites as thermoelectrics and topological insulators, *Nat. Rev. Mater.* **2**, 17049 (2017).

Supplement to Giant Anomalous Nernst Effect in Single Crystal MnBi

Bin He^{1,2,*}, Cüneyt Şahin^{3,4}, Stephen R. Boona⁵, Brian C. Sales⁶, Claudia Felser¹, Michael E. Flatté^{3,4} and Joseph P. Heremans^{2,7,8}

1. *Max Planck Institute for Chemical Physics of Solids, Dresden, 01187, Germany.*
2. *Department of Mechanical and Aerospace Engineering, The Ohio State University, Columbus OH, 43210, USA.*
3. *Pritzker School of Molecular Engineering, University of Chicago, Chicago, Illinois, 60637, USA.*
4. *Optical Science and Technology Center and Department of Physics and Astronomy, The University of Iowa, Iowa City, Iowa, 52242, USA.*
5. *Center for Electron Microscopy and Analysis, The Ohio State University, Columbus, OH, 43212, USA.*
6. *Materials Science and Technology Division, Oak Ridge National Lab, Oak Ridge, TN 37830, USA.*
7. *Department of Materials Science and Engineering, The Ohio State University, Columbus OH, 43210, USA.*
8. *Department of Physics, The Ohio State University, Columbus, OH, 43210, USA.*

1 Sample oxidation

Compared to other manganese pnictides, MnBi single crystals have limited air stability because the electronegativity of Bi is small compared to other anions. We observed that after each thermal cycling, the surface of the MnBi crystals turned slightly yellow, indicative of the formation of Bi_2O_3 . Thus, it is highly important to guarantee that the sample is mounted and measured in an air-free atmosphere to prevent sample oxidation and the accompanied weakening of the anomalous Nernst effect (ANE).

Here, we show the thermal transport properties of sample A1 over three thermal cycles. We measured the sample multiple times for reproducibility; thus, we were able to observe a clear trend that both the ANE and thermopower decrease, which can come from oxidation of the sample. When MnBi crystals are oxidized, both the Mn and Bi are able to grab oxygen from the air, forming bismuth oxide Bi_2O_3 , and complex manganese oxides (like MnO_2). This oxidation is creating defects and damaging sample quality. Oxidation of

the crystal introduces a secondary phase and changes the carrier concentration of the sample, which can significantly affect the transport properties of the crystal. Fig. S1(a) shows the thermopower of sample A1 over three cycles. We observed a decrease in thermopower as we conducted the measurements, which can result from two processes. First, as the sample is oxidized, the oxidation products may introduce extra electrons in the sample, which contributes to reducing the thermopower. Second, increased scattering of the conduction electrons or of the magnons may be induced by oxidation impurities in the material, which reduces the magnon-drag thermopower as well. As we prepared the sample for the helium cryostat measurement, the sample was oxidized significantly in the remounting process, resulting in a different temperature dependence compared to the first two cycles; this could result from the vanishing magnon-drag contribution.

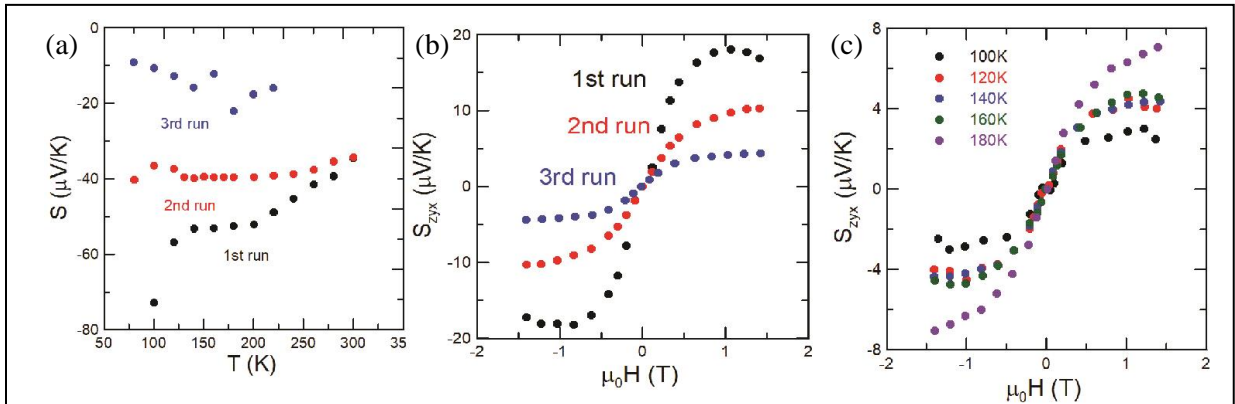


Figure S1 (a) Seebeck coefficient of A1 after thermocycling. The absolute value of the Seebeck coefficient decreases as the sample is oxidized and more defects are generated, indicative of a vanishing magnon-drag contribution. (b) Nernst thermopower after thermocycling at 100 K. Like the Seebeck coefficient, the anomalous Nernst thermopower also decreases over thermal cycles. (c) Field dependence of the third-cycle Nernst thermopower at selected temperatures. It is clear that after multiple thermal cycles, the self-SSE contribution nearly disappears, and the ANE behaves similarly to A2, with the ANE thermopower increasing with temperature.

We observed a similar result in the ANE measurement. Fig. S1(b) shows the anomalous Nernst thermopower of sample A1 at 140 K. The pristine sample had an

anomalous Nernst thermopower of $18 \mu\text{V/K}$ in the first measurement. As we thermally cycled the sample in the cryostat, the anomalous Nernst thermopower reduced to less than $10 \mu\text{V/K}$ for the second thermal cycle. After we remounted the sample for the PPMS measurement, the anomalous Nernst thermopower further reduced to about $4 \mu\text{V/K}$. As discussed above, this reduction in the ANE comes from the oxidation of the sample. The induced oxide impurities significantly eliminated the magnon-electron spin-angular momentum transfer, which can be viewed as the interface in the heterostructure SSE, leading to a smaller anomalous Nernst thermopower. For further comparison, we plot the anomalous Nernst thermopower of the third run at various temperatures in Fig. S1(c). For the third thermal cycle of sample A1, the anomalous Nernst thermopower becomes significantly smaller than the first two cycles, due to the absence of the magnon-drag induced ANE. With no magnon-drag contribution, the anomalous Nernst thermopower of A1 has the same temperature dependence as A2, which is that the ANE increases with temperature.

2 Magnetoresistance

Fig. S2 shows the cross-plane magnetoresistance (MR) of sample A1 at various temperatures, with which we calculated the anomalous Hall conductivity of A1. Unlike most magnetic materials, which have a negative MR, A1 has a small positive MR at the temperatures we measure, approximately 10% at 0.4 T. This positive MR may come from a screen effect from the itinerant electrons. Sample A2 has the identical MR as A1, while the in-plane sample B1 has negligible MR, compared to A1 and A2.

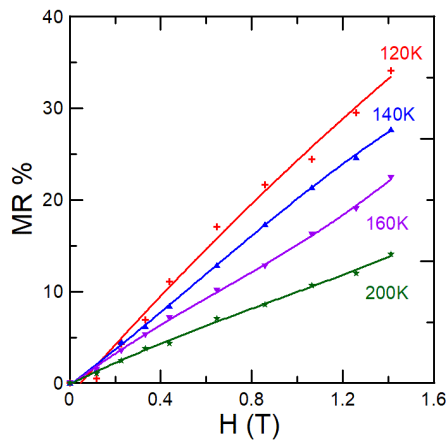


Figure S2: magnetoresistance of sample A1 at various temperatures.

3 Hysteresis

Fig. S3(a) and (b) show the hysteresis curve of Hall and Nernst effect on sample A1 during the first run. We select the data at 140 K as an example, and at other temperatures, the results are similar to the 140 K result. In both Hall and Nernst

measurements, we did not observe hysteresis.

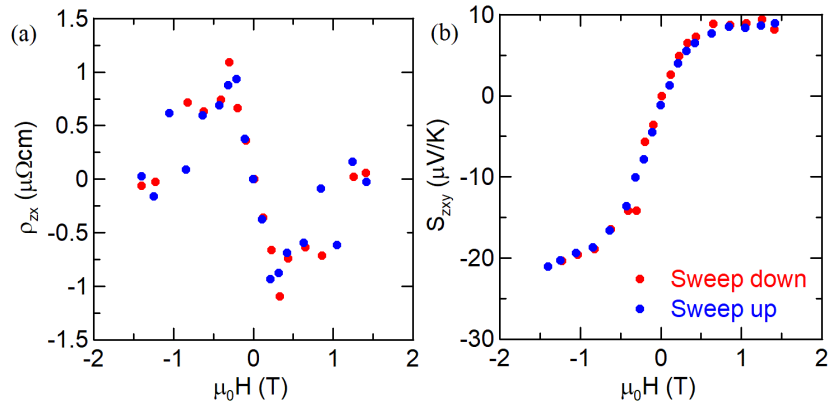


Figure S3: Hysteresis of transverse properties (a) Hall resistance (with longitudinal resistance subtracted) (b) Nernst thermopower.